Spatially resolved degradation during startup and shutdown in polymer electrolyte membrane fuel cell operation

Komini Babu, Siddharth
Spernjak, Dusan
Dillet, J.
Lamibrac, A.
Maranzana, G
Didierjean, S.
Lottin, O.
Borup, Rodney L.
Mukundan, Rangachary

To be published in: Applied Energy

DOI to publisher's version: 10.1016/j.apenergy.2019.113659

‘Spatially Resolved Degradation during Startup and Shutdown in Polymer Electrolyte Membrane Fuel Cell Operation

S. Komini Babu[a,*], D. Spernjak[a], J. Dillet[b], A. Lamibrac[b,c], G. Maranzana[b], S. Didierjean[b], O. Lottin[b], R. L. Borup[a], and R. Mukundan[a]

[a] Los Alamos National Laboratory, Los Alamos, NM 87545, USA
[b] LEMTA, CNRS, and Université de Lorraine, Vandoeuvre-lès-Nancy, France
[c] Present address: Department of Biomedical Engineering, University of Basel, Switzerland
* Corresponding author: skb@lanl.gov

Polymer electrolyte membrane fuel cells have durability limitations associated with the startup and shutdown of the fuel cell, which is critical for real-world vehicle commercialization. During startup or shutdown, there exists an active region (hydrogen/air) and a passive region (air/air) between the cell inlet and outlet. Internal currents are generated in the passive region causing high-potential excursion in the cathode leading to accelerated carbon corrosion. In this study, a segmented cathode hardware is used to evaluate the effect of platinum loading on both cathode and anode, and carbon support material on degradation due to repeated series of startups or shutdowns. *In situ* losses in the performance and electrochemical surface area were measured spatially, and *ex situ* analysis of the catalyst layer thickness and platinum particle size was performed to understand the effect of startup or shutdown on different membrane electrode assembly materials. Startup degrades the region near anode outlet more, while shutdown degrades the region near anode inlet more compared to the rest of the electrode. While various system mitigation strategies have been reported in the literature to limit this degradation, one materials mitigation strategy is to limit the anode's ability to reduce oxygen to water through increasing the ratio of platinum loading in the cathode to the anode, or by using a bi-functional catalyst.

Introduction

Reduction of greenhouse gas emission is crucial to reduce global warming and in particular from the transportation sector as it amounts for a third of CO_2 emission in the United States. Electric vehicles based on polymer electrolyte membrane (PEM) fuel cells which utilize hydrogen as fuel are zero emission vehicles with high energy density and quick refueling. PEM fuel cells have been shown to be a viable replacement for conventional technologies in the transportation sector with the release of Toyota Mirai and several prototypes from other automotive manufacturers (GM, Ford, Nissan, Hyundai, etc.). However, cost and durability requirements are still barriers to widespread commercialization. US DOE durability targets for automotive and stationary applications are 5000 h and 60000 h, respectively. Several studies have shown automotive fuel cell degradation [1], including start/stop of fuel cell[2]. Hence, much work in the past decade has focused on improving the durability of PEM fuel cell components [3], protocols for testing durability [4] and

developing mitigation strategies [5]. However, the lifetime test is long and expensive, and therefore, there is a need for a better understanding of the degradation mechanisms and the establishment of accelerated stress tests (AST) for the various cell components [6]. Instead of targeting single cell components, some more complex ASTs are carried out at the cell or stack level to investigate the degradation mechanisms linked with common but delicate operating conditions such as steady-state (constant current or voltage) or potential/load cycling [7], start-up/shut-down cycles [8], hydrogen starvation with a dead-ended anode[9], temperature cycling, and even freeze/thaw protocols [10].

Several degradation mechanisms reduce the performance and hence the durability of the fuel cell. Electrochemical carbon oxidation to carbon dioxide (carbon corrosion) at the cathode has been identified as one of the leading reasons for performance degradation. Carbon corrosion leads to a reduction in electrode porosity, loss in the catalyst electrochemical surface area (ECSA), change in carbon wettability and loss in electrical contact. Cell reversal, startup (SU), shutdown (SD), operating potential, and fuel (H_2) starvation are few of the conditions that give rise to carbon corrosion and the combination of these phenomena could lead to accelerated carbon corrosion. The cell operating conditions that give rise to carbon corrosion are well known [11], but the mechanism of carbon corrosion is still being studied to develop material mitigation strategies [5]. Since the anode fuel is pure hydrogen, the anode potential will be maintained at ~ 0 V vs. reference hydrogen electrode (RHE), and the cathode catalyst layer potential will be between 0.6 V – 1.0 V, depending on the operating conditions. SU/SD transients occur in the presence of both the fuel (H_2) and the oxidant (O_2/air) in the anode and magnitude of the local anode electrolyte potential at the hydrogen-starved region increases leading to the cathode interfacial potential vs electrolyte experiencing values higher than 1.2 V [12].

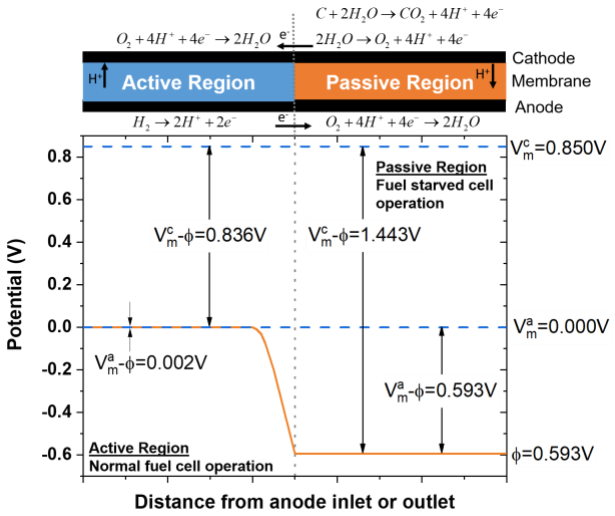

Figure 1. Electrolyte potential distribution during H_2-starved operations. Electrolyte potential shifts along the channel where fuel is available (active region) and the fuel-starved portion (passive region) during SU/SD. (Figure recreated from ref. [12])

During SU/SD, the anode region can be compartmentalized into sections that are hydrogen-filled and hydrogen-starved. Reiser et al. proposed a mechanism for the degradation due to H_2 starvation in the passive region shown in Figure 1 [12]. In the active region, the hydrogen oxidation reaction (HOR) and oxygen reduction reaction (ORR) occur in the anode and cathode respectively. In the passive region, air (O_2) in the anode undergoes

reduction to water, and Pt undergoes oxidation and reduction during SD and SU respectively. Air (O_2) in the fuel-starved anode causes ORR in the anode and shifts the reference potentials leading to water splitting in the cathode along with the oxidation of carbon to carbon dioxide (CO_2), thus generating currents from the active region (hydrogen-filled) to the passive region (hydrogen-starved). In the active region, the anode potential $\left(V_m^a\right)$, vs. the electrolyte potential (Φ) is at zero (which is the equilibrium potential of H_2), and the net cell voltage is increased to the cathode potential $\left(V_m^c\right)$. However, in the passive region, the same anode potential is maintained because of high electronic conductivity, which leads to lowering of Φ in the passive region to maintain the potential close to the equilibrium potential of O_2 due to the presence of air (O_2). This high potential in the passive region leads to carbon corrosion and CO_2 evolution degrading the catalyst layer. The H^+ generated during the oxidation reactions occurring at the cathode, such as the oxygen evolution reaction (OER) and the carbon oxidation, transport to the anode for the ORR. This is termed as reverse current [12]. The degradation due to the carbon corrosion in the passive region can be mitigated by reducing the time of air/air (O_2/O_2) operation in the anode, and corrosion-resistant support in the cathode. The regions in the cathode that experience high potentials due to local starvation of fuel, show an increase in carbon corrosion rates. Carbon corrosion is more detrimental to the catalyst layer compared with other components, such as the gas diffusion layer (GDL), due to the availability of proton conducting pathways and the presence of the catalyst, platinum.

To characterize carbon corrosion, prior publications focused on CO_2 emissions [13], ECSA, post-mortem analyses[14], and the performance of the entire fuel cell [15]. However, in a membrane electrode assembly (MEA) there also exists a spatial difference, where the carbon corrosion occurs due to the presence of active and passive regions. The corrosion is accelerated in the region where high potential excursions occur due to air/air operation as described above [16]. During SU, the fuel introduction at the inlet in the anode filled with air (O_2) leads to a H_2/air front at the inlet progressing towards the outlet. The region near the outlet experiences maximum time in the passive region, leading to higher degradation compared to the inlet. Similarly, during SD the inlet experiences maximum time in air/air operation, leading to increased degradation at the inlet compared to the outlet. Hence there is a need to characterize the effect of SU/SD on the MEA spatially through the cell. Specialized segmented hardware has been used previously to characterize the performance and temperature of a fuel cell spatially [17]. The University of Lorraine has developed segmented hardware to measure current distribution in a fuel cell [18]. This hardware has been used to test the effect of the SU/SD AST protocols [16], and also to study the effect of system mitigation strategies [19]. Measuring the reverse current and correlating it to in situ measurements (performance, ECSA, CO_2 emissions) and ex situ characterization (scanning electron microscope [SEM], transmission EM, X-ray diffraction [XRD]) can be valuable for a better understanding of degradation caused by carbon corrosion from SU/SD. Also, such correlations can be helpful for providing inputs to durability models for improved predictive capabilities. Maranzana et al. developed a computational model to explain the internal current and provide mitigation strategies for SU/SD [20]. There are several materials, hardware, and electronic control strategies to mitigate the detrimental effects of SU/SD transients, but understanding how SU/SD affects the components is vital, as the mitigation strategies might give rise to other degradation mechanisms in addition to increased cost [21].

In this work, we used the hardware that was previously designed and built at the University of Lorraine to decouple the effect of SU/SD on the various components in the MEA [16]. We previously reported data from *in situ* testing in ref. [16]. Additional *in- situ* tests are encompassed in the present work to include MEAs with different types of carbon support and weight percentage of the Pt catalyst. More importantly, focus is placed on the material characterization of the MEAs presented here as well as those reported in ref. [16], which was not presented in our previous publication. The segmented cell was used to conduct local *in situ* measurements of voltage, polarization curves, and electrochemical surface area (ECSA) at different segments from the inlet to the outlet. We used separate AST for SU and SD, which decouple their effects. To characterize the carbon loss, we also measured the CO_2 evolution at the cathode using non-dispersive infrared (NDIR) and the thinning of the catalyst layer via SEM. The Pt particle size was examined via XRD at both inlet and outlet after SU/SD protocol. To elucidate the effect of Pt loading on SU/SD, different Pt loadings in both anode and cathode catalyst layers were examined. Also, the effect of the cathode catalyst support was examined, along with varying the cathode thickness by utilizing catalysts with different Pt/C weight ratios. This study for the first time intimately couples in situ and ex situ characterization of carbon corrosion in a segmented fuel cells to elucidate the contribution of different degradation modes (Pt coarsening, carbon loss) to performance loss during SU/SD, and suggests materials mitigation strategies to minimize this degradation.

Experimental

Hardware

The segmented hardware used in this work, shown in Figure 2, has been described in detail in our previous work [16]. In brief, the hardware active area is 1 cm x 30 cm with five parallel channels in both the anode and cathode flow fields. The land and channel widths are 1 mm each on both anode and cathode. The depth of the channel is 0.5 mm and 0.7 mm in the anode and the cathode respectively. The cathode active area is divided into 20 segments along the channel. Flow in the cell is in counterflow configuration, such that segment #1 corresponds to the air inlet and H_2 outlet at the cathode and anode, respectively. Similarly, segment #20 corresponds to the air outlet and H_2 inlet at the cathode and anode, respectively.

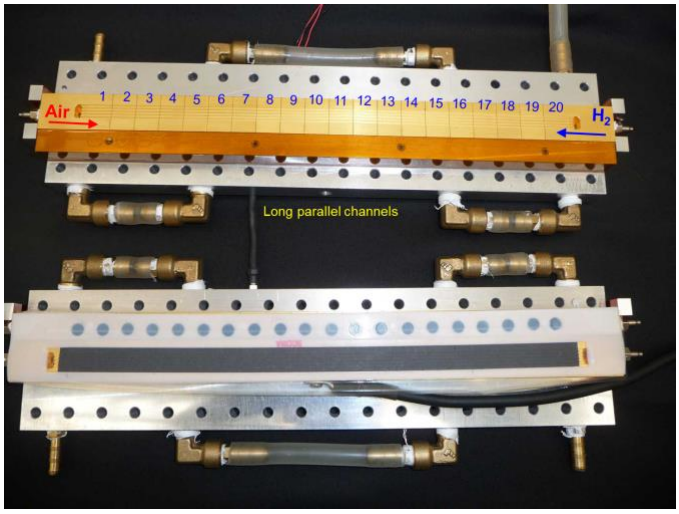

Figure 2. The segmented hardware with 20 segments in the cathode (top) and the anode flow field plate (bottom). The flow field consists of 5 parallel channels in a counter flow configuration. (Figure reprinted with permission from Ref.[18])

AST Protocols for SU and SD

The protocols for the accelerated stress tests (AST) used in this work are separate for SU and SD to decouple their individual effects on degradation and carbon corrosion. Figure 3 shows the breakdown of individual steps within a startup and a shutdown cycle, including durations, gas types, and flow rates for each step. The cell was operated at 80 ^{o}C, no back pressure, and 90 % RH unless stated otherwise. The anode and cathode flow stoichiometry during normal operating conditions were 1.5 and 3.5, respectively.

In the SU protocol, as shown in Figure 3a, the cell is operated in H_2/air for 300 s at a constant current of 0.67 A cm^{-2} followed by a 10s open circuit voltage (OCV) hold. Before introducing air into the anode, the cell is shut down (or, purged) using 20 slph (standard liters per hour) of N_2 for 60 s to minimize the effect of SD in the SU AST protocol. At the startup of the SU AST, H_2 is introduced in the air-filled anode, and a 10 s OCV hold follows before the cycle is repeated.

In the SD protocol, shown in Figure 3b, after normal cell operation for 300 s, air is introduced for 120 s at 10 slph. The anode is then filled with N_2 to minimize the effect of SU. At the start of the SD AST, H_2 is introduced in the nitrogen-filled anode for 180s at 90 slph.

At the beginning of life (BOL), and in between every 30 cycles of SU for startup testing(or SD for shutdown testing), the fuel cell was characterized. The set of 30 cycles is termed a sequence. The sequence was repeated until the ECSA was reduced to 50 % of the BOL ECSA. Depending on the material the sequence was repeated between 10 and 32 times, as shown in Table 1. The N_2 purge step in the protocol is to ensure the effects of the SU or SD are not mixed even though in an actual operating fuel cell their effects are combined. The full extent of combined SU and SD is not the focus of this study.

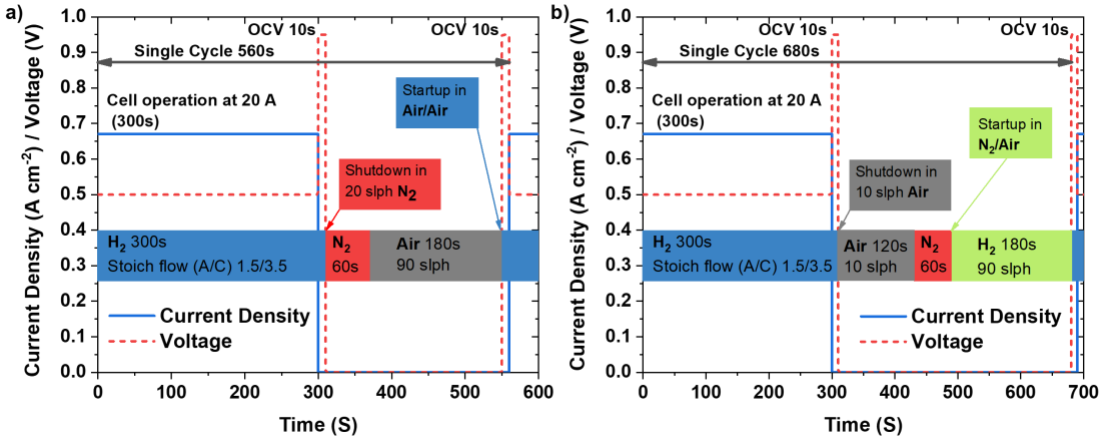

Figure 3. AST protocol for a single cycle corresponding to a) SU and b) SD. The single cycle repeated 30 times is a sequence, and the MEA is characterized before the start of each sequence. The sequence is repeated until the ECSA loss is 50 %.

Materials

In this study, MEAs were fabricated by Ion Power Inc. (Delaware, USA) with commercial TKK catalysts. Six different specifications of MEAs with various Pt loading, Pt/C ratio, and carbon support were fabricated. Table 1 shows the MEA specifications used in this study as well as the MEA identifier. The reference MEA, used as a baseline in this study, had a cathode/anode loading of 0.27/0.09 mg_{Pt} cm^{-2} (measured by X-ray fluorescence [XRF]) prepared from 40 weight (wt.) % Pt on Vulcan (TEC10V40E). Effect of Pt loading on the degradation was examined by using two MEAs with either the high cathode or anode Pt loading fabricated with the same catalyst as the reference MEA. MEA with high surface area carbon (HSAC) support with different wt.% of Pt, 20 wt.% (TEC10E20E), and 40 wt.% (TEC10E40E) Pt on carbon respectively was fabricated to study the effect of the catalyst support as well as catalyst layer thickness. Low surface area carbon (LSAC), with highly graphitized carbon support, was also fabricated using 40 wt.% Pt on carbon (TEC10EA40E). Nafion® XL (DuPont, Wilmington, DE) was used as the membrane in all the MEAs for this study. The anode catalyst in all the MEAs was prepared from 40 wt.% Pt on Vulcan. Both the anode and cathode catalyst were coated directly on to the membrane. The GDL in both anode and cathode was SGL 24BC (SGL carbon, Germany) for all MEAs.

Due to the time-consuming nature of SU and SD experiments, repeated tests were conducted with a limited subset of materials and testing protocols. For more details see our earlier paper [16] (Section 5. Reproducibility and uncertainty of the experimental results).

TABLE 1. Catalyst Specification of different MEAs used in this study.

Electrode	Description	Anode Loading (mg_{Pt} cm^{-2})	Cathode Loading (mg_{Pt} cm^{-2})	Ratio of Cathode to Anode Loading	Pt Wt. %	Cathode Support	Cathode Catalyst
Reference	Reference	0.09	0.27	3.00	40	Vulcan	TEC10V40E
High Pt Cathode	High cathode loading	0.09	0.61	6.78	40	Vulcan	TEC10V40E
High Pt Anode	High anode loading	0.18	0.31	1.72	40	Vulcan	TEC10V40E
High Surf C 20 wt.%	High surface area carbon with 20 wt.% Pt	0.05	0.17	3.40	20	HSAC	TEC10E20E
High Surf C 40 wt.%	High surface area carbon with 40 wt.% Pt	0.09	0.24	2.67	40	HSAC	TEC10E40E
High Graphitized C	High graphitized carbon	0.09	0.12	1.33	40	LSAC	TEC10EA40E

Characterization

The MEAs were first conditioned by cycling 50 times through the following cycle:

1. Holding at a constant voltage of 0.6 V for 45 s;
2. Open circuit for 30 s;

3. Holding at a constant voltage of 0.3 V for 60 s.

For each MEA, *in situ* characterization included the measurement of polarization curves, the voltage at a constant current hold at 0.67 A cm^{-2}, and the ECSA, between each set of SU or SD sequences for each segment of the MEA. During the SU/SD sequence, the CO_2 evolution was measured for the entire cathode. To measure carbon loss, a non-dispersive infrared (NDIR) sensor (NDIR gas analyzer 603D by California Analytical Instruments, with dual range of 50 and 500 ppm and resolution of 1% of the range) was connected in line to the cathode exhaust after a water trap (condenser and desiccant column) to measure the CO_2 concentration. The NDIR data was used to calculate the total carbon loss in each sequence using the following formulation:

$$\left\langle C\ loss\left(\mu g\right)\right\rangle = \frac{A_c Q_{std} P_{std}}{R T_{std}} \int \left(ppm\ CO_2 \right) dt \tag{1}$$

where A_c is the atomic weight of carbon, Q_{std} is the total volumetric flow rate in slpm, P_{std} and T_{std} are standard pressure and temperature respectively, and R is the ideal gas constant. Note that the carbon loss calculated only includes the carbon lost that was fully oxidized to CO_2 in the MEA.

Catalyst layer (CL) thickness and Pt particle size were measured using *ex situ* characterization (SEM, X-ray diffraction (XRD)) for both BOL and end of life (EOL). At EOL, samples were characterized at H_2 outlet and inlet to study spatial variations in degradation. XRD (Siemens D5000, Cu k-a radiation) was used to measure the Pt particle size by carefully scraping the CL after removing the GDL. The MEA cross-section was imaged, and CL thickness was measured using an SEM. The MEA samples for SEM were prepared by freezing in a liquid nitrogen bath and subsequently cutting the cross-section of an MEA sample.

Result and Discussion

Effect of SU/SD AST on MEA

The ECSA measured during the SU/SD AST protocol is shown in Figure 4. Table 2 shows the ECSA at BOL and EOL for SU/SD for all the MEAs listed in Table 1. In SU AST cycles, the cathode with highly graphitized support had the lowest ECSA loss rate (ΔECSA/ Δ#cycles) of 0.02 and 0.01 $m^2\ g^{-1}\ cycle^{-1}$ for SU and SD, which is similar to the high cathode loading MEA (0.02 and 0.01 $m^2\ g^{-1}\ cycle^{-1}$ for SU and SD, respectively). The MEA with higher anode Pt loading had a faster cathode ESCA loss rate (0.07 and 0.04 $m^2\ g^{-1}\ cycle^{-1}$ for SU and SD, respectively) than the reference MEA (0.05 and 0.04 $m^2\ g^{-1}\ cycle^{-1}$ for SU and SD respectively) and the MEA with higher cathode Pt loading. HSAC support with 40 Pt wt.% had a higher loss rate (0.06 and 0.04 $m^2\ g^{-1}\ cycle^{-1}$ for SU and SD, respectively) than the reference MEA, which had Vulcan carbon support. However, the HSAC support with lower Pt wt.% (20 wt.%) had the highest loss rate of 0.105 and 0.06 $m^2\ g^{-1}\ cycle^{-1}$ for SU and SD, respectively. It should also be noted that 20 wt.% Pt on HSAC support MEAs had low anode and cathode loading. The highly graphitized carbon showed the lowest initial Pt ECSA. At BOL, the initial ECSA for SU and SD varies for the same type of MEA; this might be due to the slight variations in the MEAs and the cell assembly.

The ECSA loss rate is higher for SU compared to SD for all the MEA materials tested as reported previously for a few of the MEAs [16].

CO_2 emissions at the cathode is a measure of the carbon lost from the cathode due to carbon corrosion. The CO_2 emission for all the MEAs during both SU and SD have a higher initial rate which decreases with subsequent protocol sequences. CO_2 emissions due to carbon corrosion are in general higher during the SU than during the SD protocol, as shown in Figure 5, consistent with the loss in ECSA. Highly graphitized carbon support (LSAC) shows one of the lowest starting CO_2 evolution rates in both the SU and SD experiments. Graphitized carbon has the lowest surface area and hence lower defect sites for carbon corrosion, but the carbon loss increases with cycling. The graphitized carbon might be changing its properties during cycling leading to increasing CO_2 emissions, unlike other MEAs where carbon loss decreases with time. During SU, the HSAC support regardless of the Pt wt.% has a higher carbon loss than the reference MEA, which used Vulcan support. The HSAC has higher defect sites compared to Vulcan, which is vulnerable to degradation, increasing the rate of carbon loss. MEA with higher Pt loading in the cathode has the lowest carbon corrosion, while increasing the anode Pt loading increases the carbon loss. In fact, doubling the anode loading of a Vulcan carbon MEA results in its carbon emission being comparable to that of an HSAC-based MEA (a 2x increase). Higher Pt loading in the anode increases the ORR rate, generating higher reverse current (to consume the protons generated by carbon corrosion) and hence accelerating the degradation. When carbon emissions are normalized to the BOL carbon loading, the emissions are lowest for the MEA with high cathode loading. MEA with 40 wt.% Pt on HSAC and high anode loading both have higher carbon loss compared to the reference MEA, as shown in Table 2. During the SD, the carbon loss is similar for all MEAs except the MEA with high graphitized support. When normalized to their initial carbon loading, the loss is similar except for the MEA with HSAC support with 40 wt.% Pt and the high graphitized MEA. The initial high CO_2 emission rates followed by a reduction in the rates could be due to the loss of carbon, which is both electronically and ionically connected, for carbon corrosion. At BOL, the surface of carbon that is connected to Pt, accessible to water, and bound well by ionomer will corrode first, after which the lower available volume of this connected carbon will reduce the rate of carbon loss with cycling. The Pt/C ratio and the type of carbon do affect the connectivity of the carbon to platinum and ionomer, and given a particular catalyst type, the CL loading just increases the thickness of the catalyst layer. Therefore, higher loaded carbons are not expected to have better connectivity and are not expected to corrode more. Also, at BOL the CL may contain more unstable Pt particles and carbon, which are more susceptible to corrosion. The rapid decrease in CO_2 is also attributed to the increased ratio of graphitized to amorphous carbon, continuing passivation of carbon due to partial oxidation, and Pt particle agglomeration [16].

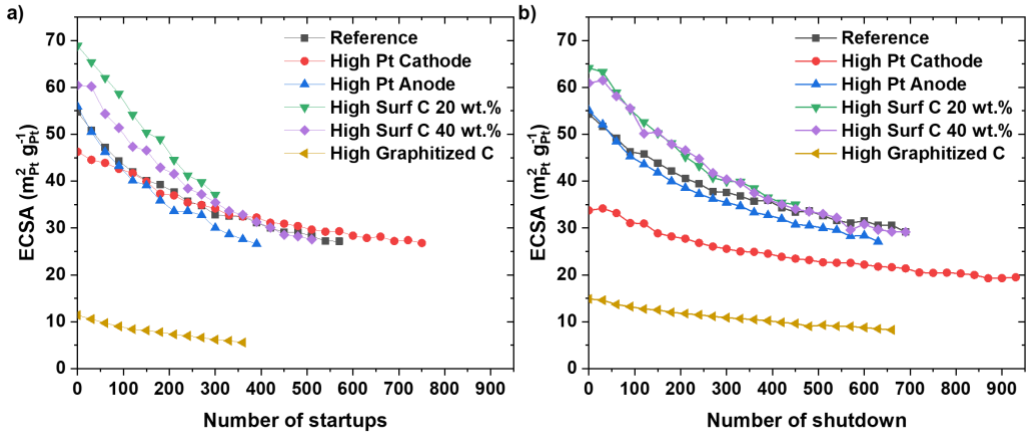

Figure 4. The loss of electrochemical surface area measured after each sequence of a) SU and b) SD AST protocol. The operating conditions are 80 °C, 90% RH, and zero back pressure. Partial data was previously presented in Ref. [16].

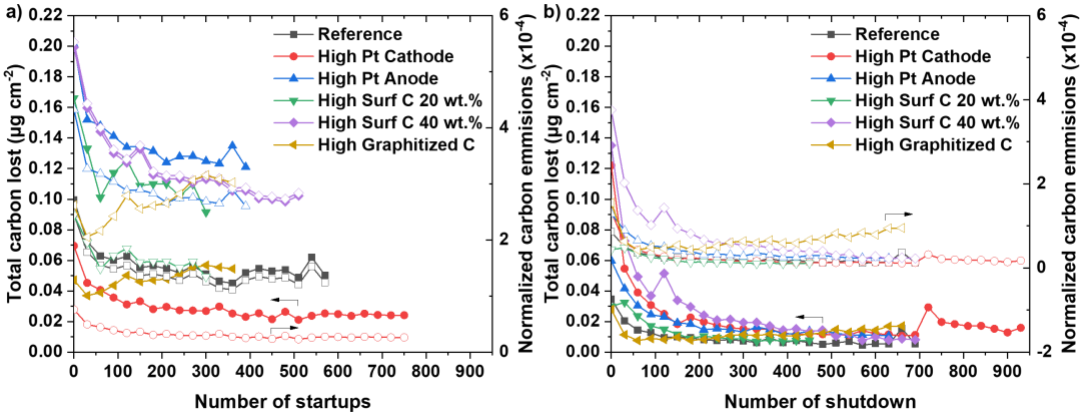

Figure 5. Carbon loss measured from CO_2 evolution in cathode per sequence of a) SU and b) SD AST protocol. Solid symbols are the total carbon lost, and open symbols are total carbon loss normalized to the BOL carbon loading. The operating conditions are 80°C, 90% RH, and zero back pressure. Partial data was previously presented in Ref. [16].

Voltage decay at a fixed current density (0.67 A cm^{-2}) as a function of SU/SD sequence cycles is shown in Figure 6 for all the MEAs in Table 1. Figure 6 illustrates that SU is more detrimental to performance than SD, as the voltage degrades faster in SU compared to SD cycling. Compared to the reference MEA (Vulcan support), the HSAC support has a higher performance loss. The MEA with the highest ratio of cathode to anode loading showed the lowest degradation rates, consistent with the previous ECSA loss and carbon emissions. At BOL, the voltage is lower for the highly graphitized carbon, and the voltage loss is highest during both SU and SD, as shown in Table 2. In all MEAs the performance loss is a combination of the Pt particle growth, due to agglomeration and migration, as well as carbon corrosion, which causes loss in performance even after the CO_2 emission has decreased. The loss in performance for the highly graphitized support MEA is probably not only due to carbon corrosion as the carbon loss is lower than other MEAs which have

very low voltage decay rates but also change in Pt particle size (which is discussed in a later section).

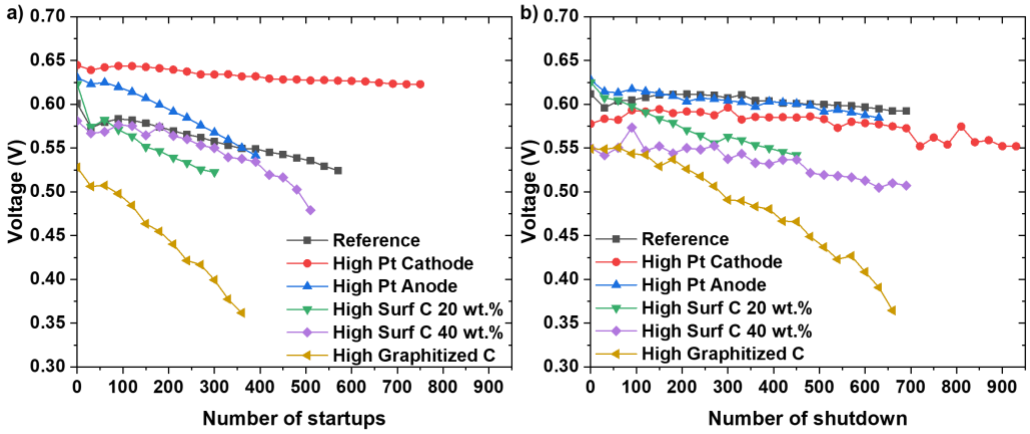

Figure 6. Voltage decay at a constant current of 0.67 A cm^{-2} for different MEA materials due to a) SU and b) SD. The number of cycles performed for each AST protocol for each MEAs is given in Table 2. The operating conditions are 80°C, 90% RH, and zero back pressure. Partial data was previously presented in Ref. [16].

TABLE 2. Total voltage and carbon loss for the different MEAs listed in Table 1.

Electrode	Number of cycles (# sequences)		Voltage at 0.67 A cm^{-2} (V)						Carbon loss	
	SU	SD	SU			SD			SU	SD
			BOL	EOL	Loss (%)	BOL	EOL	Loss (%)	Total Carbon loss (μg cm^{-2})	Total Carbon loss (μg cm^{-2})
Reference	570 (19)	690 (23)	0.60	0.52	13	0.61	0.59	3	1.15	0.23
High cathode loading	750 (25)	930 (31)	0.64	0.62	3	0.58	0.55	5	0.76	0.69
High anode loading	390 (13)	630 (21)	0.63	0.54	14	0.63	0.58	7	1.93	0.41
High surface area carbon 20 wt.% Pt	300 (10)	450 (15)	0.62	0.52	16	0.63	0.54	14	1.28	0.21
High surface area carbon 40 wt.% Pt	510 (17)	690 (23)	0.58	0.48	17	0.55	0.50	9	2.18	0.65
High graphitized carbon	360 (12)	660 (22)	0.53	0.36	32	0.55	0.37	32	0.63	0.28

To summarize the results from Figures 4–6, SU is more detrimental than SD. The cathode with higher Pt loading and Vulcan carbon support (TEC10V40E) had the lowest voltage degradation, carbon loss, and ECSA loss rate. Higher anode Pt loading had the reverse effect compared to higher cathode loading, resulting in higher performance loss. The higher Pt in the anode provides a higher ORR current in the passive region (air/air operation), which increases the reverse current, thereby increasing the degradation in the cathode by high potential excursion. In this regard, we showed in a previous study that the choice of the MEA materials had a significant impact on the local current density during SU or SD, while the maximum cathode potential was not strongly affected [22]. Similarly, in the cathode with the higher Pt loading, the ratio of loading in the cathode to anode is high compared to the reference MEA and this might have a similar effect due to the low Pt in the anode. Thus, to prevent and/or reduce the reverse current, one mitigation strategy is to limit the anode's ability for ORR by reducing the Pt loading in the anode or using a

higher ratio of Pt loading in the cathode to the anode. HSAC support had a higher voltage degradation rate and CO_2 emission, but the ECSA loss was similar to the reference MEA that had Vulcan support. Vulcan support, in general, had lower degradation due to lower defects susceptible to carbon corrosion and higher graphitization compared to HSAC. The degradation is similar for different Pt wt.% on HSAC support.

The MEA with highly graphitized carbon support has lower ECSA and carbon loss; however, when normalized to the initial carbon loading, it indicates higher carbon loss. It should also be noted that the MEA with highly graphitized carbon support had lower loading at both anode and cathode. The graphitized support (LSAC) is better at preventing carbon loss but still shows a significant performance loss during the SU/SD cycles; the causes of this performance loss we speculate as poor Pt adhesion to the carbon, as will be discussed in the post-characterization section. The lower initial performance, Figure 6, does not make it a practical option for commercial MEAs. The results from voltage decay, carbon loss, and ECSA decrease suggest lower and higher Pt loading at the anode and cathode, respectively, with Vulcan support would reduce the degradation due to SU/SD. Other mitigation strategies include using a bi-functional anode catalyst that would promote hydrogen evolution reaction (HER) and suppress the ORR. This is necessary as the new state-of-the-art MEAs have a total Pt loading of lower than 0.125 mg_{Pt} cm^{-2} and hence, higher cathode loading is not a viable option to meet cost targets.

<u>In situ spatial measurements along the gas channel</u>

Here we discuss the spatial difference observed due to SU/SD gas fronts on different MEAs. Figures 7 and 8 show the ECSA loss along the channel length for all the MEAs measured after each sequence of SU (top row) and SD (bottom row) protocol. The color scheme is used to distinguish between different numbers of SU or SD cycles. Hydrogen flow direction is denoted by an arrow. Dotted lines are added to each graph to indicate the different ECSA loss at inlet vs. outlet qualitatively.

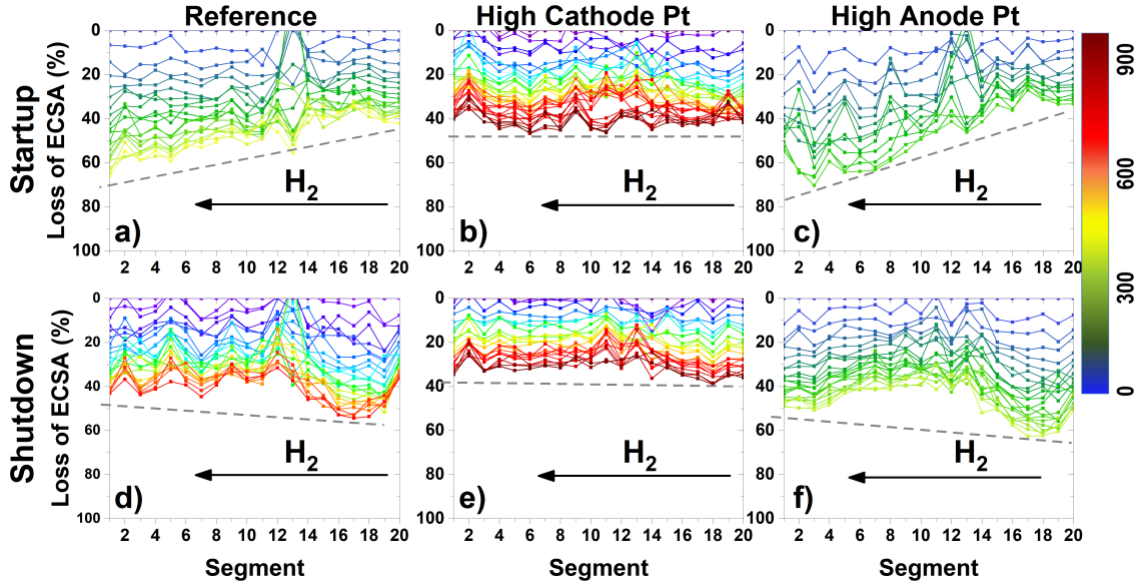

Figure 7. ECSA loss along the channel segments for SU (a, b, c) and SD (d, e, f) AST protocol at different sequences for reference MEA (a, d), high cathode Pt loading (b, e), and high anode loading (c, f). Segment 1 represents air inlet/H_2 outlet; Segment 20

represents the air outlet/H_2 inlet. High cathode Pt shows a minimal loss in ECSA and minimal variation in ECSA along the segments. The operating conditions are 80°C, 90% RH, and zero back pressure. Color bars represent the numbers of sequences.

In general, during SU the segments close to the cathode inlet/anode outlet (segment 1) and during SD the segments close to the cathode outlet/ anode inlet (segment #20) showed the most ECSA loss. This is due to longer residence time in the passive region (air/air), causing increased degradation and ECSA loss. The MEA with high cathode Pt loading (Figure 7b and 7e) was an outlier compared to other MEAs as the degradation loss was more uniform along the length of the channel, i.e., little variation between inlet and outlet. The high anode Pt loading MEA had a higher variation in ECSA loss, a much higher ECSA loss in both SU and SD than the reference MEA in addition to the higher difference between inlet and outlet as shown in Figures 7c and 7f. During SU, the ECSA loss along the channel at EOL is similar between the reference and high anode loading MEA but the number of cycles is longer for the reference MEA. HSAC support MEAs (Figure 8a, 8b, 8d, and 8e) had high ECSA loss and distribution of ECSA loss along the channel showed localized spots for degradation (channel segments where ECSA loss is lower than the surrounding segments). The 40 wt.% Pt on HSAC support MEA showed a higher difference in ECSA loss, similar to high anode loading Pt MEA, between inlet and outlet compared to 20 wt.% Pt MEA. The MEA with 20 wt.% Pt on HSAC support had lower C/A loading ratio compared to the reference and 40 wt.% on HSAC support. Note that highly graphitized carbon showed a similar trend to most MEAs, but the H_2 outlet in the case of SU and H_2 inlet in the case of SD showed lower degradation than the rest of the segments. The highly graphitized support MEA showed high ECSA loss similar to high anode loading MEA, whose C/A loading ratio is similar to the highly graphitized MEA. The low ECSA loss at the inlet during SD might be due to end cell effect where the H_2 can diffuse to the inlet manifold resulting in decreased corrosion from segment 19 and 20.

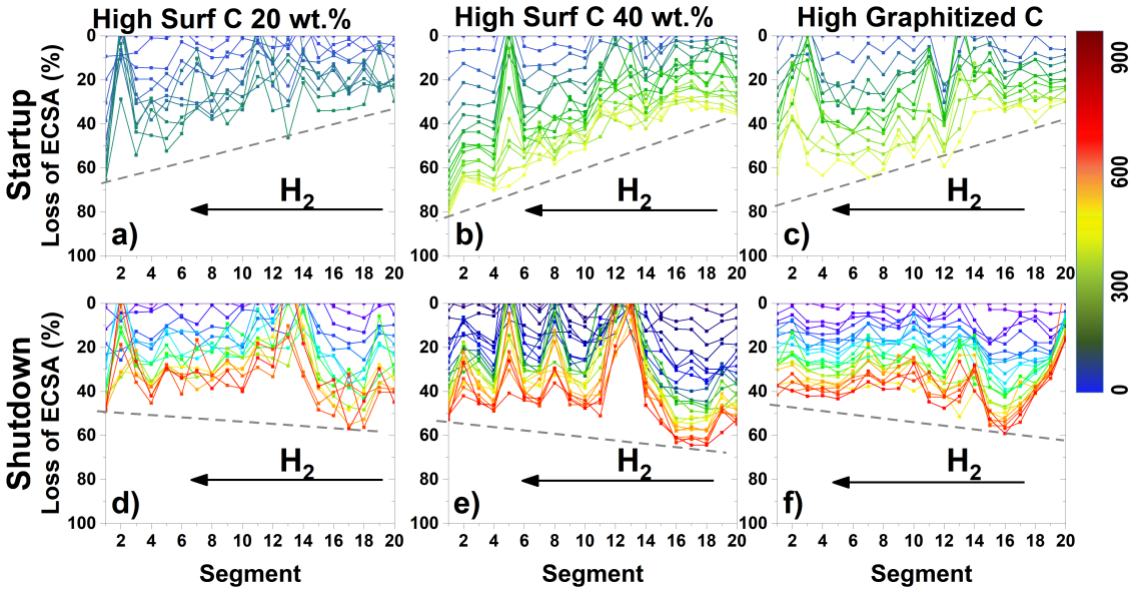

Figure 8. ECSA loss along the channel segments for SU (a, b, c) and SD (d, e, f) AST protocol at different sequences for HSAC support with 20 wt.% Pt (a, c), 40 wt. % Pt (b, d), and highly graphitized carbon (c, e) support. Segment 1 represents air inlet/H_2 outlet; Segment 20 represents the air outlet/H_2 inlet. High surface area carbon support shows a higher variation in the ECSA loss along the segments and the 40 wt. % shows the highest

ECSA loss between inlet and outlet. The operating conditions are 80ºC, 90% RH, and zero back pressure. Color bars represent the numbers of sequences.

Spatial measurement of polarization curves is shown in Figure 9 for SU and SD for the reference MEA. The current density was higher at the air inlet (Figure 9b, 9e) and was lower at the air outlet (Figure 9c, 9f) due to the difference in air pressure and O_2 concentration along the channel. As expected during SU, the anode outlet has higher performance decrease (Figure 9b) than the inlet (Figure 9c) due to longer exposure time in air/air. This is in accordance with the observed ECSA loss (Figure 7). At the H_2 inlet, there is no performance loss observed between 300 and EOL due to the dominant mechanism being Pt migration and agglomeration, which is consistent with the high initial ECSA loss observed (Figure 4 and Figure 7a). As observed previously, the SD (Figure 9d) does not show as much degradation in the performance compared to SU (Figure 9a). Similarly, the measured performance during SD showed more decrease at the H_2 inlet (Figure 9f) than the H_2 outlet (Figure 9e). The measured high-frequency resistance (HFR) does not change from BOL to EOL, suggesting that the membrane and interfacial resistances did not change during the carbon corrosion.

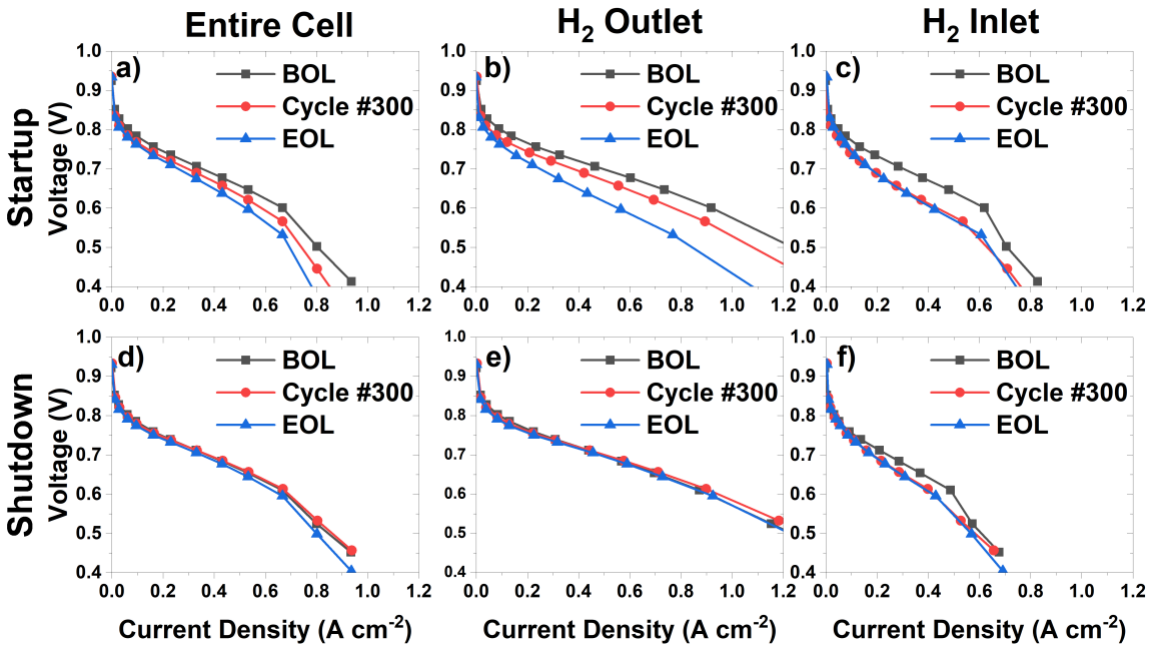

Figure 9. Reference MEA polarization curve during SU (a, b, c) and SD (d, e, f) for the entire cell (a, d), segment #2/H_2 outlet (b, e), and segment #19/H_2 inlet (c, f). Number of cycles at EOL stated in Table 2. The operating conditions are 80ºC, 90% RH, and zero back pressure.

Polarization curves for MEAs with HSAC and 40 wt.% Pt at EOL and BOL are shown in Figure 10 for the SU and SD AST protocol. The performance loss at H_2 outlet for the HSAC (Figure 10b) is significantly higher than the performance loss observed in the reference MEA (Figure 9b). This is consistent with previously observed ECSA loss (Figure 4), performance loss (Figure 6), and CO_2 emissions (Figure 5). During SD, the performance loss at the H_2 inlet (Figure 10f) is higher than the reference MEA (Figure 9f) as HSAC is highly susceptible to carbon corrosion compared to the Vulcan carbon support used in the reference MEA. Although the performance loss for the entire cell appears similar, there is

significant loss in the kinetic region (0.8 V). The measured HFR values do not change during the AST protocol which is consistent to reference MEA. Other MEAs exhibit similar trends to the reference MEA except for highly graphitized MEA where significant performance loss is observed at both H_2 inlet and outlet for SU/SD protocol. Note, the performance at BOL for SU and SD is different and might be due to variation in MEA or experimental error. The polarization curve for the MEA with high anode loading is shown in Figure 11 at the H_2 inlet and outlet, as well as the overall performance. During SU AST protocol, the polarization curve at the H_2 inlet (Figure 11b) showed significant performance compared to H_2 inlet. This trend is consistent with that previously observed for 40 wt.% Pt on HSAC MEA. However, during SD the polarization curve (Figure 11f) showed higher performance loss than the reference and the 40 wt.% Pt on HSAC MEA. This is consistent with the previously observed ECSA loss, CO_2 emission, and voltage decay (Figure 4–6).

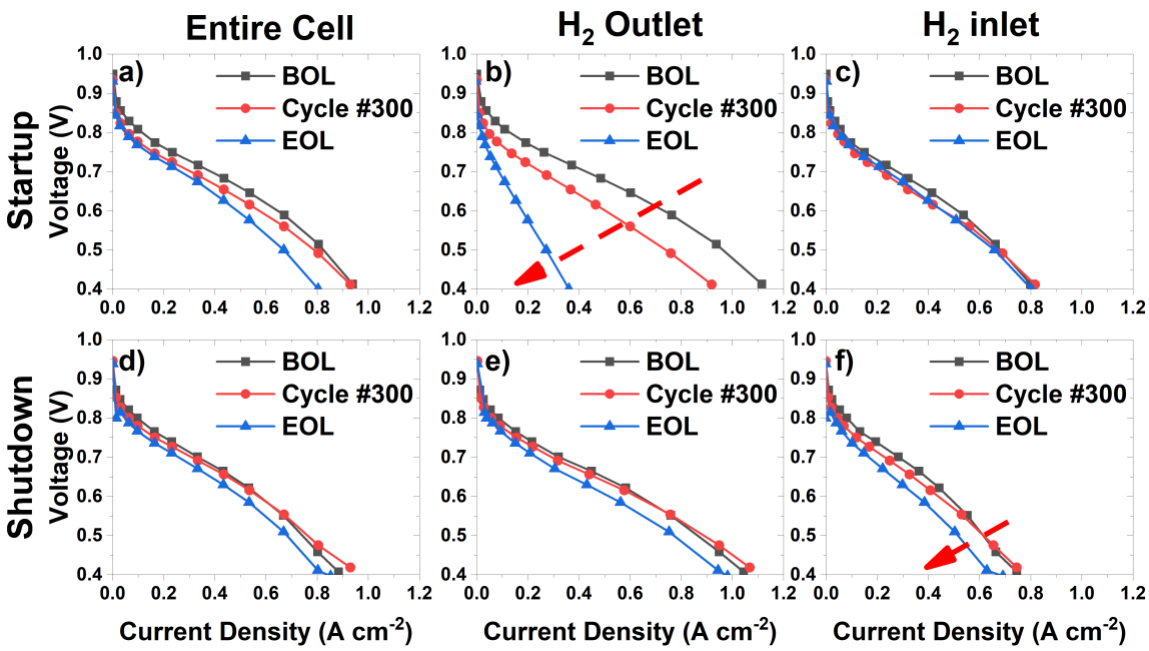

Figure 10. Polarization curve of HSAC support with 40 wt. % Pt MEA during SU (a, b, c) and SD (d, e, f) for the entire cell (a, d), segment #2/H_2 outlet (b, e), and segment #19/H_2 inlet (c, f). The operating conditions are 80°C, 90% RH, and zero back pressure.

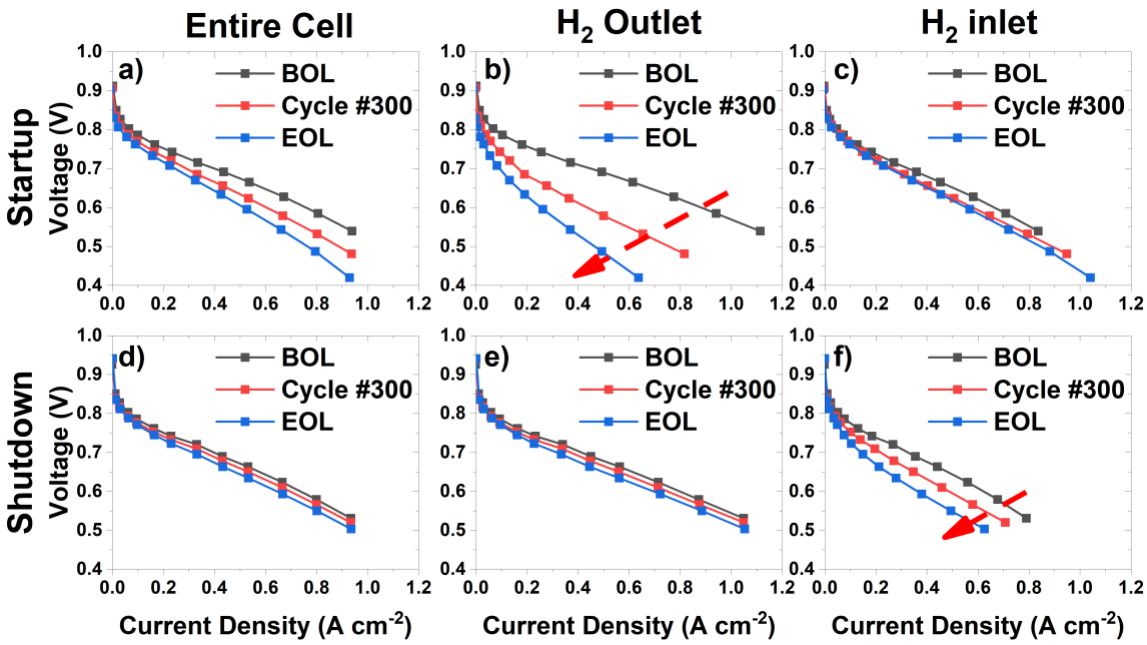

Figure 11. High anode Pt loading MEA polarization curve during SU (a, b, c) and SD (d, e, f) for the entire cell (a, d), segment #2/H_2 outlet (b, e), and segment #19/H_2 inlet (c, f). The operating conditions are 80°C, 90% RH, and zero back pressure.

Ex situ spatial measurements

Ex situ characterization of the MEA for both SU and SD is shown in Figure 12. Pt particle size (Figure 12a) of the cathode was measured using XRD, at BOL and spatially (outlet and inlet) at EOL after the series of SU and SD AST protocols. In general, the Pt particle size for all MEAs at BOL was smaller than at EOL possibly due to Pt particle growth during SU/SD. After SU, the Pt particle size was larger at the H_2 outlet compared to the H_2 inlet. Similarly, after SD, the Pt particle size was larger at the H_2 inlet. This is consistent with the previously observed results of ECSA loss. The increase in particle size could be due to Pt migration, Ostwald ripening, and particle coalescence [23]. Pt particle growth might possibly be occurring more during the initial sequences where there might be many more unstable Pt particles and carbon support. This also could explain the initial rapid degradation observed in the voltage decay (Figure 6), CO_2 emission (Figure 5), and the ECSA loss (Figure 4). The Pt particle size measured from XRD is highly consistent with ECSA data [24]. Potential cycling alone could result in particle growth, even if there is little carbon corrosion (MEAs with high cathode Pt loading) and this seems to be the predominant mechanism of degradation for the high loaded MEA which was operated for the longest time (least carbon corrosion). It has been previously reported that degradation by 1.2 V hold AST results in carbon corrosion and Pt particle size growth for different carbon supports (Vulcan, HSAC and, LSAC) [25]. However, for all the other MEAs the differences between H_2 inlet and outlet are consistent with the cell regions that experience greater/longer air/air passive operation indicating that the dominant mechanism is linked to carbon corrosion. Pt particle size in MEA with 40 wt.% Pt on HSAC support was similar to reference MEA and HSAC support with 20 wt.% Pt showed lower Pt particle size than reference MEA. It should be noted that the 20 wt.% Pt on HSAC support MEA had a lower C/A loading ratio than 40 wt.% Pt with HSAC support MEA. MEA with LSAC support showed higher Pt particle size similar to MEA with high Pt loading anode with Vulcan support, which could be due to the poor adhesion of the Pt to the support, unlike then high

anode loading case where Pt detachment from the support due to the corrosion leads to an increase in particle size. Both the MEA with the highly graphitized support and the high anode loading MEA had low C/A loading ratio. The MEAs that exhibited substantial ECSA loss between inlet and outlet (high Pt loading anode, 40 wt.% Pt on HSAC support) also showed a significant difference in Pt particle size.

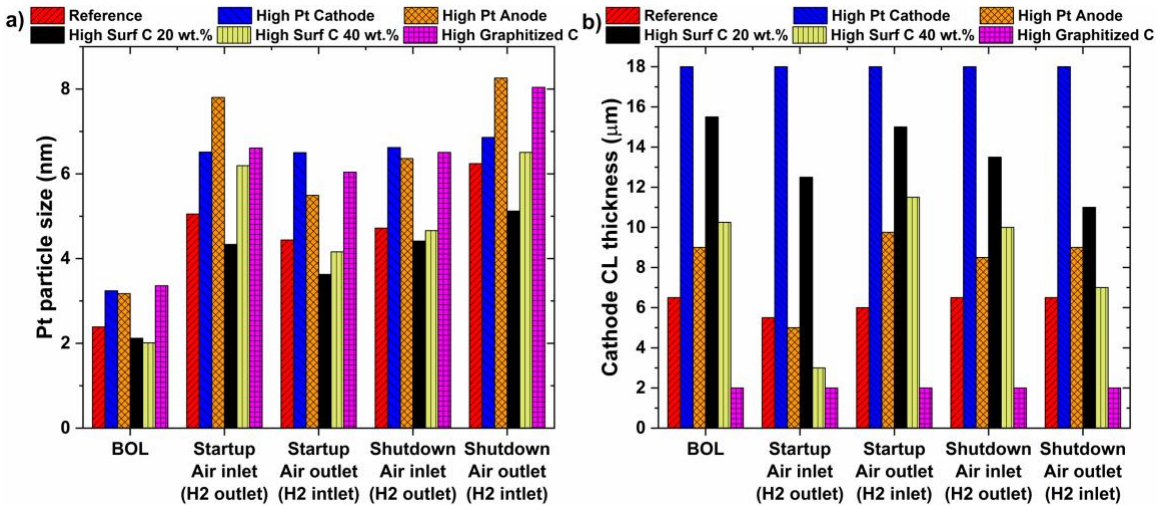

Figure 12. Change in a) Pt particle size measured from XRD and b) cathode CL thickness change at BOL and EOL measured from SEM. EOL analysis is performed at H_2 inlet and outlet for both SU and SD.

Figure 12b shows the cathode CL thickness after the SU and SD protocols. The difference in CL thickness between inlet and outlet for SU is larger than SD, which is consistent with the previous results. The reference MEA with Vulcan support showed a nominal decrease in CL thickness after SD, with low carbon loss. The MEA with high Pt cathode does not show any reduction in CL thickness for both SU and SD, which is consistent with the lowest carbon corrosion (Figure 5) and ECSA loss (Figure 4). While thickness is constant for the MEA with high Pt loading, the Pt particle size does show a large increase consistent with the even ECSA loss across the MEA (Figure 7b). This indicates that the Pt particle size also increases due to voltage cycling which is not linked with carbon corrosion and the larger particle size is due to more number of SU/SD cycles than other MEAs tested. In contrast, the MEA with high anode Pt loading showed 4 μm difference in CL thickness between inlet and outlet during SU AST. The CL with HSAC support and 20 wt.% Pt showed minimal thinning compared to the 40 wt.% Pt on HSAC MEA, possibly due to lower C/A loading ratio. The MEA with the HSAC support and 40 wt.% Pt showed significant thinning of the CL (Figure 13), which is consistent with the carbon loss (Figure 5) and the decrease in performance measured spatially (Figure 10). This might be due to increased catalyzing carbon corrosion and facilitating Pt agglomeration (shorter Pt-Pt distance) due to increased Pt/C ratio. Figure 13a shows the BOL cross-section and the average cathode CL thickness of 11 μm for the 40% Pt on HSAC MEA. MEA cross-section at EOL at H_2 outlet is shown in Figure 13b and illustrates the thinning of the CL to 3 μm from 11 μm initially. In general, thinner CLs (given the same Pt loading) have more Pt agglomeration as there are more Pt particles per carbon to catalyze the corrosion reaction. The MEA with the graphitized carbon support is very thin (2 μm) and shows mass transport problems as seen in the poor initial voltage. Similar to the MEA with the high Pt loaded cathode, the MEA with graphitized support does not show

any CL thinning, which is consistent with the lack of significant carbon loss during SU and SD. Electrodes with carbon loss less than 1 percent, from Table 2, still show significant CL thinning, suggesting a significant loss in porosity due to compaction leading to increased mass transport resistance (which is observed in the polarization curve in Figure 10).

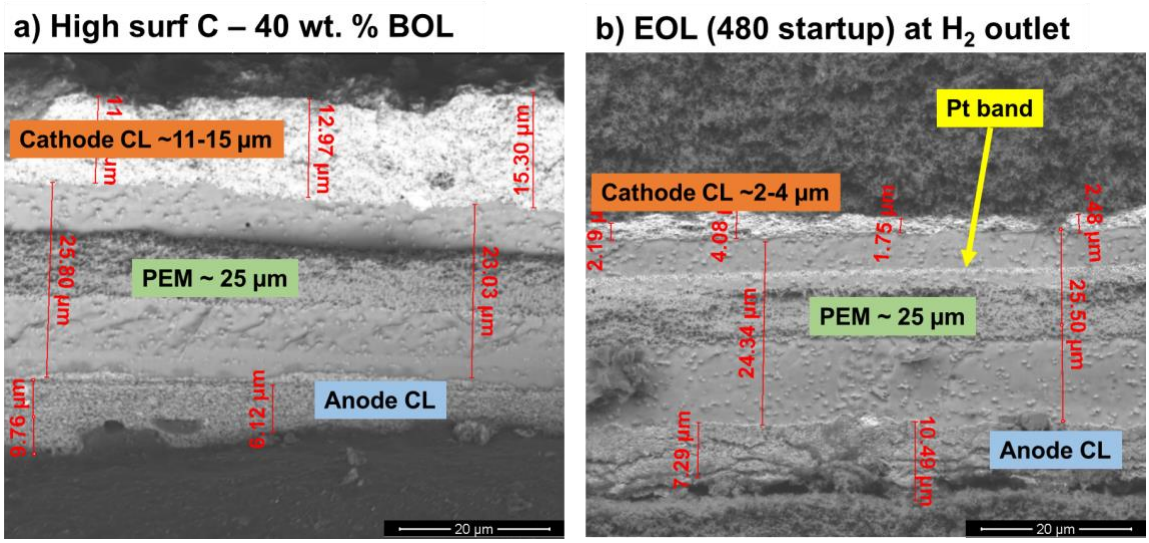

Figure 13. CL thickness at H_2 outlet of HSAC support with 40 wt. % Pt MEA at a) BOL and b) EOL (after 480 SU cycles).

Our results suggest SU is more detrimental than SD, but there could be other conditions where SD is more detrimental than SU. This could occur if the residence time in the passive region during SD is higher than in SU, or if the SU temperature is significantly lower than the SD temperature. In the current study, during SU and SD AST protocols the cell was at 80°C. However, in an actual operation, SU will be at low temperature and SD at high temperature, which can lead to SD being more detrimental than SU. Hardware (flow field layout and dimensions), operating conditions (flow rate, relative humidity), and materials (GDL, CL porosity) can significantly affect the flow of gases and hence the residence time of air/O_2 in the passive region. Dillet et al. showed carbon loss reduces significantly upon increasing the gas flow rate [16]. In-plane differences in the material in the land and the channel region were observed and attributed to lower diffusion under the land [26].

Conclusions

Degradation and performance decay were spatially resolved in a 1-dimensional segmented polymer electrolyte fuel cell. The cell was subjected to accelerated stress testing consisting of repeated startups or shutdowns. In both startup and shutdown there is non-uniform degradation between inlet and outlet regions of the fuel cell, as the residence time in the passive region would create high-potential excursions in the cathode, leading to localized hot spots for degradation. Startups were more detrimental to the fuel cell than shutdowns. Startups from air-air where the incoming hydrogen takes longer to displace the air, increases its residence time in the passive region, leading to increased carbon corrosion. In situ measurements of voltage decay, carbon dioxide evolution measurement, and electrochemical surface area loss as a function of the cycle of startup- or shutdown-

accelerated stress testing protocol agreed well for the various catalyst types. There is a correlation between spatially measured local electrochemical surface area loss, polarization degradation, platinum growth, and cathode catalyst layer thinning. There is platinum particle size increase with very minimal associated carbon corrosion due to voltage cycling, confirmed by no loss in thickness of the catalyst layer and even electrochemical surface area loss across the membrane electrode assembly. However, this is not as severe as the platinum electrochemical surface area loss associated with platinum agglomeration due to carbon support corrosion confirmed by the lower number of cycles needed to have 50% loss in electrochemical surface area than the membrane electrode assembly that exhibited electrochemical surface area loss with minimal carbon corrosion.

From the different membrane electrode assemblies tested, lower degradation during the startup or shutdown protocols was recorded for higher platinum loading in the cathode while reducing the anode platinum loading. Lower platinum loading in the anode reduces the reverse current by limiting oxygen reduction reaction at the anode and hence reduces the carbon corrosion. Also, since the current on the anode must be balanced by opposing current on the cathode, keeping the ratio of platinum loading in the cathode to anode high helps to limit the damage due to cathode carbon corrosion during startup or shutdown. The membrane electrode assembly with a higher platinum loading in anode showed an increased degradation rate, higher carbon loss rates, and electrochemical surface area loss. Higher platinum loading in the anode causes an increased rate of oxygen reduction reaction in the anode that can support a greater proton current generated by carbon oxidation at the cathode, accelerating the degradation. High platinum loading in the anode showed significant loss in catalyst layer thickness and large increase in platinum particle size compared to reference and the high cathode loading membrane electrode assembly.

The catalyst support type and the platinum on carbon weight percentage affect the rates of degradation as well. Membrane electrode assemblies with high surface area carbon support showed lower durability than the reference membrane electrode assembly which used Vulcan support. At end of life, the 40 wt.% platinum on high surface area carbon support has considerable cathode catalyst layer thinning due to carbon corrosion (and compaction, i.e., pore space collapse), and high platinum growth than reference membrane electrode assembly which has Vulcan support as platinum adheres well to the defects in high surface area carbon. Membrane electrode assembly with high surface area carbon support and 20 wt.% platinum showed lower platinum particle growth and catalyst layer thinning compared to the membrane electrode assembly with 40 wt.% platinum due to increased distance between platinum particles and higher defects in high surface area carbon for platinum to adhere. Carbon corrosion rate is also increased as more platinum in contact with carbon catalyzes the corrosion. The 20 wt.% membrane electrode assembly also had a lower cathode to anode loading ration than the 40 wt.% membrane electrode assembly. Membrane electrode assembly with highly graphitized carbon support has less thinning (carbon support more stable, lower carbon dioxide emission) while still exhibiting significant platinum growth, similar to high anode loading membrane electrode assembly, since platinum is not well adhered to the relatively defect-free graphitized carbon. Membrane electrode assembly with highly graphitized carbon also had a low cathode to anode loading ratio, similar to the high anode loading membrane electrode assembly.

Acknowledgments

Members of the group from Los Alamos National Laboratory wish to acknowledge the funding from the US Department of Energy, the Office of Energy Efficiency and Renewable Energy, Fuel Cell Technologies Office, and the support of the technology development manager Nancy Garland and fuel cell team leader Dimitrios Papageorgopoulos. Members of the group from Lorraine University and CNRS wish to acknowledge the funding from Région Lorraine and CNRS.

The authors also acknowledge SGL Carbon GmbH for supplying the GDL materials, and Ion Power for fabricating the MEAs. We thank Greg James and Mark Watson of Ballard Power Systems for useful discussions regarding the development of startup/shutdown protocols.

Glossary

AST	Accelerated Stress Tests
BOL	Beginning of Life
CL	Catalyst Layer
ECSA	Electrochemical Surface Area
EOL	End of Life
GDL	Gas Diffusion Layer
HFR	High-frequency Resistance
HER	Hydrogen Evolution Reaction
HOR	Hydrogen Oxidation Reaction
HSAC	High Surface Area Carbon
LSAC	Low Surface Area Carbon
MEA	Membrane Electrode Assembly
NDIR	Non-Dispersive Infrared
OCV	Open Circuit Voltage
OER	Oxygen Evolution Reaction
ORR	Oxygen Reduction Reaction
PEM	Polymer Electrolyte Membrane
RHE	Reference Hydrogen Electrode
SD	Shutdown
SEM	Scanning Electron Microscope
SU	Startup
XRD	X-ray Diffraction

References

[1] Wang J. System integration, durability and reliability of fuel cells: challenges and solutions. Applied Energy. 2017;189:460-479.
[2] Zhang T, Wang P, Chen H, Pei P. A review of automotive proton exchange membrane fuel cell degradation under start-stop operating condition. Applied Energy. 2018;223:249-262.
[3] Borup R, Meyers J, Pivovar B, Kim YS, Mukundan R, Garland N, Myers D, Wilson M, Garzon F, Wood D, Zelenay P, More K, Stroh K, Zawodzinski T, Boncella J, McGrath JE, Inaba M, Miyatake K, Hori M, Ota K, Ogumi Z, Miyata S, Nishikata A, Siroma Z, Uchimoto Y, Yasuda K, Kimijima K-i, Iwashita N. Scientific Aspects of Polymer Electrolyte Fuel Cell Durability and Degradation. Chemical Reviews. 2007;107:3904-3951.

[4] Chen H, Song Z, Zhao X, Zhang T, Pei P, Liang C. A review of durability test protocols of the proton exchange membrane fuel cells for vehicle. Applied Energy. 2018;224:289-299.
[5] Wu J, Yuan XZ, Martin JJ, Wang H, Zhang J, Shen J, Wu S, Merida W. A review of PEM fuel cell durability: Degradation mechanisms and mitigation strategies. Journal of Power Sources. 2008;184:104-119.
[6] Zhang S, Yuan X, Wang H, Mérida W, Zhu H, Shen J, Wu S, Zhang J. A review of accelerated stress tests of MEA durability in PEM fuel cells. International Journal of Hydrogen Energy. 2009;34:388-404.
[7] Gaumont T, Maranzana G, Lottin O, Dillet J, Didierjean S, Pauchet J, Guétaz L. Measurement of protonic resistance of catalyst layers as a tool for degradation monitoring. International Journal of Hydrogen Energy. 2017;42:1800-1812.
[8] Bae SJ, Kim SJ, Park JI, Park CW, Lee JH, Song I, Lee N, Kim KB, Park JY. Lifetime prediction of a polymer electrolyte membrane fuel cell via an accelerated startup-shutdown cycle test. International Journal of Hydrogen Energy. 2012;37:9775-9781.
[9] Abbou S, Dillet J, Maranzana G, Didierjean S, Lottin O. Local potential evolutions during proton exchange membrane fuel cell operation with dead-ended anode – Part I: Impact of water diffusion and nitrogen crossover. Journal of Power Sources. 2017;340:337-346.
[10] Petrone R, Hissel D, Péra MC, Chamagne D, Gouriveau R. Accelerated stress test procedures for PEM fuel cells under actual load constraints: State-of-art and proposals. International Journal of Hydrogen Energy. 2015;40:12489-12505.
[11] Pei P, Chen H. Main factors affecting the lifetime of Proton Exchange Membrane fuel cells in vehicle applications: A review. Applied Energy. 2014;125:60-75.
[12] Reiser CA, Bregoli L, Patterson TW, Yi JS, Yang JD, Perry ML, Jarvi TD. A Reverse-Current Decay Mechanism for Fuel Cells. Electrochemical and Solid-State Letters. 2005;8:A273-A273.
[13] Spernjak D, Fairweather J, Mukundan R, Rockward T, Borup RL. Influence of the microporous layer on carbon corrosion in the catalyst layer of a polymer electrolyte membrane fuel cell. Journal of Power Sources. 2012;214:386-398.
[14] De Moor G, Bas C, Caqué N, Maranzana G, ElKaddouri A, Perrin J-C, Chatenet M, Lamibrac A, Maillard F, Moukheiber E, Dubau L, Castanheira L, Dillet J, Flandin L, Lottin O. A review of PEM fuel cell durability: materials degradation, local heterogeneities of aging and possible mitigation strategies. Wiley Interdisciplinary Reviews: Energy and Environment. 2014;3:540-560.
[15] Mittermeier T, Weiß A, Hasché F, Gasteiger HA. PEM Fuel Cell Start-Up/Shut-Down Losses vs Relative Humidity: The Impact of Water in the Electrode Layer on Carbon Corrosion. Journal of The Electrochemical Society. 2018;165:F1349-F1357.
[16] Dillet J, Spernjak D, Lamibrac A, Maranzana G, Mukundan R, Fairweather J, Didierjean S, Borup RL, Lottin O. Impact of flow rates and electrode specifications on degradations during repeated startups and shutdowns in polymer-electrolyte membrane fuel cells. Journal of Power Sources. 2014;250:68-79.
[17] Yu Y, Yuan XZ, Li H, Gu E, Wang H, Wang G, Pan M. Current mapping of a proton exchange membrane fuel cell with a segmented current collector during the gas starvation and shutdown processes. International Journal of Hydrogen Energy. 2012;37:15288-15300.
[18] Abbou S, Dillet J, Spernkak D, Mukundan R, Fairweather J, Borup RJ, Maranzana G, Didierjean S, Lottin O. Time Evolution of Local Potentials during PEM Fuel Cell Operation with Dead-Ended Anode. ECS Transactions. 2013;58:1-1.

[19] Abbou S, Dillet J, Spernjak D, Mukundan R, Borup RL, Maranzana G, Lottin O. High Potential Excursions during PEM Fuel Cell Operation with Dead-Ended Anode. Journal of The Electrochemical Society. 2015;162:F1212-F1220.
[20] Maranzana G, Lamibrac A, Dillet J, Abbou S, Didierjean S, Lottin O. Startup (and Shutdown) Model for Polymer Electrolyte Membrane Fuel Cells. Journal of the Electrochemical Society. 2015;162:F694-F706.
[21] Yu Y, Li H, Wang H, Yuan X-Z, Wang G, Pan M. A review on performance degradation of proton exchange membrane fuel cells during startup and shutdown processes: Causes, consequences, and mitigation strategies. Journal of Power Sources. 2012;205:10-23.
[22] Lottin O, Dillet J, Maranzana G, Abbou S, Didierjean S, Lamibrac A, Borup RL, Mukundan R, Spernjak D. Experimental Results with Fuel Cell Start-up and Shut-down. Impact of Type of Carbon for Cathode Catalyst Support. ECS Transactions. 2015;69:1065-1074.
[23] Shao-Horn Y, Sheng WC, Chen S, Ferreira PJ, Holby EF, Morgan D. Instability of supported platinum nanoparticles in low-temperature fuel cells. Topics in Catalysis. 2007;46:285-305.
[24] Mukundan R. Accelerated Testing Validation. US DOE FCT Program Annual Merit Review and Peer Evaluation Meeting. 2014.
[25] Mukundan R, James G, Ayotte D, Davey JR, Langlois D, Spernjak D, Torraco D, Balasubramanian S, Weber AZ, More KL, Borup RL. Accelerated Testing of Carbon Corrosion and Membrane Degradation in PEM Fuel Cells. ECS Transactions. 2013;50:1003-1010.
[26] Durst J, Lamibrac A, Charlot F, Dillet J, Castanheira LF, Maranzana G, Dubau L, Maillard F, Chatenet M, Lottin O. Degradation heterogeneities induced by repetitive start/stop events in proton exchange membrane fuel cell: Inlet vs. outlet and channel vs. land. Applied Catalysis B: Environmental. 2013;138-139:416-426.